Imaging nuclear modifications on parton distributions with triple-differential dijet cross sections in proton-nucleus collisions

Shuwan Shen,[1] Peng Ru,[2,3,*] and Ben-Wei Zhang[1,2,†]

[1]*Key Laboratory of Quark and Lepton Physics (MOE) and Institute of Particle Physics, Central China Normal University, Wuhan 430079, China*

[2]*Guangdong Provincial Key Laboratory of Nuclear Science, Institute of Quantum Matter, South China Normal University, Guangzhou 510006, China*

[3]*Guangdong-Hong Kong Joint Laboratory of Quantum Matter, Southern Nuclear Science Computing Center, South China Normal University, Guangzhou 510006, China*

(Received 11 January 2022; accepted 4 May 2022; published 24 May 2022)

Dijet production in proton-nucleus (pA) collisions at the LHC provides invaluable information on the underlying parton distributions in nuclei, especially the gluon distributions. Triple-differential dijet cross sections enable a well-controlled kinematic scan (over momentum fraction x and probing scale Q^2) of the nuclear parton distribution functions (nPDFs), i.e., $f_i^{\mathrm{A}}(x, Q^2)$. In this work, we study several types of triple-differential cross sections for dijet production in proton-proton and proton-lead (pPb) collisions at the LHC, to next-to-leading order within the framework of perturbative quantum chromodynamics (pQCD). Four sets of nPDF parametrizations, EPPS16, nCTEQ15, TUJU19, and nIMParton16 are employed in the calculations for pPb collisions. We show that the observable nuclear modification factor $R_{p\mathrm{Pb}}$ of such cross sections can serve as a nice image of the nuclear modifications on parton distributions, quantified by the ratio $r_i^{\mathrm{A}}(x, Q^2) = f_i^{A,\mathrm{proton}}(x, Q^2)/f_i^{\mathrm{proton}}(x, Q^2)$. Considerable differences among the $R_{p\mathrm{Pb}}$ predicted by the four nPDF sets can be observed and intuitively understood. Future measurements of such observables are expected to not only constrain the nPDF parametrizations, but also help confirm various nuclear effects, e.g., shadowing, antishadowing, EMC, and Fermi motion in different regions of x and their variations with probing scale Q^2.

DOI: 10.1103/PhysRevD.105.096025

I. INTRODUCTION

Nuclear parton distribution functions (nPDFs) are indispensable nonperturbative inputs in the study of various hard-scattering processes in high-energy nuclear collisions [1,2], including lepton-nucleus, hadron-nucleus, and nucleus-nucleus collisions. Due to the additional dynamics that bind nucleons together, the partonic structure of a large nucleus can obviously deviate from that of the free nucleons [3–9]. To exactly determine this deviation will not only help understand the interactions among bound nucleons, but also provide a baseline to precisely study other physics, such as the final-state jet quenching phenomena in hot and dense quark-gluon plasma in relativistic nucleus-nucleus collisions [10,11].

The deviations of the nuclear parton distributions from the free-proton ones are usually quantified with the ratios $r_i^{\mathrm{A}}(x, Q^2) = f_i^{A,\mathrm{proton}}(x, Q^2)/f_i^{\mathrm{proton}}(x, Q^2)$, which are generally functions of the nuclear mass number A, parton flavor i, momentum fraction x, and the resolution scale Q^2. Currently, there exist many parametrized nPDF sets determined through the global analysis of world experimental data [12–23], based on the factorization in perturbation theory of quantum chromodynamics (QCD). However, differences among the factors $r_i^A(x, Q^2)$ given by these nPDF sets can be observed, and their uncertainties are still considerable [1].

Before the running of the Large Hadron Collider (LHC), the main data sources of the global extraction are from lepton deeply-inelastic scattering (DIS) off the nucleus and the Drell-Yan (DY) process in hadron-nucleus collisions. In both of them, a detailed scan of nPDFs over x and Q^2 can be achieved by controlling the final-state kinematic variables. For example, in DIS the conventional two variables are Bjorken x_B and photon virtuality, and in DY the invariant mass and rapidity of dilepton are typically chosen [24]. Nevertheless, both DIS and DY are largely sensitive to the quark distributions, but provide less direct constraints

*p.ru@m.scnu.edu.cn
†bwzhang@mail.ccnu.edu.cn

on gluon distribution. Thus, the uncertainty of the nuclear correction $r_i^A(x, Q^2)$ on gluon distribution is usually greater than that of the quark distribution [13]. Although some early global analyses have taken into account the pion data from the Relativistic Heavy Ion Collider (RHIC), which are more sensitive to the nuclear gluon distribution, the unavoidable fragmentation functions may introduce an additional theoretical uncertainty in the determination of nPDFs [25].

The wealthy data from the LHC have significantly promoted the extraction of nPDFs. For example, the production of weak boson through DY process provides a new insight into nuclear quark distributions at a high resolution scale [7,26–29]. In particular, powerful constraints on nuclear gluon distribution are given by the productions of dijets [25,30] and heavy-quark mesons (J/Ψ, D^0, etc.) [21,31,32] in proton-nucleus (pA) collisions, with which both shadowing and antishadowing effects on gluons have been more consolidated [21,30–32].

Dijet production in pA collisions at the LHC has rich yields and has been well studied within perturbative QCD [33–39]. Moreover, the theoretical calculations do not rely on fragmentation functions. Thus, it is an important probe of both the quark and gluon distributions in nuclei [40,41]. However, since the dynamic channels for dijet production are more complicated than those in DIS and DY, a detailed scan of the nPDFs over x and Q^2 may not be easily achieved by controlling only two kinematic variables of dijet. In contrast, a better correspondence to x and Q^2 can be established by simultaneously fixing three dijet variables, which has motivated the idea to study the triple-differential dijet cross sections [35,39,42] instead of the double-differential ones. So far, this idea has been applied in proton-proton (pp) collisions to study the proton PDFs [35,39,42]. As will be discussed in this paper, the triple-differential dijet cross sections have more advantages in pA collisions for unveiling the nuclear corrections of PDFs.

In this work, we will study several types of triple-differential dijet cross sections in both pp and pA collisions to next-to-leading order (NLO) within pQCD. Four sets of nPDFs, EPPS16 [17], nCTEQ15 [15], TUJU19 [18], and nIMParton16 [16] are used in the calculations of pA. We show that the nuclear modification factors R_{pA} of the triple-differential cross sections can well disclose the x and Q^2 dependence of the nPDF factors $r_i^A(x, Q^2)$ of quark and gluon distributions, and can even serve as a nice image of the $r_i^A(x, Q^2)$ from small to large values of x. This in turn provides an intuitive way to understand the observed differences among the R_{pA} predicted by various nPDFs.

The rest of this paper is organized as follows. In Sec. II we review the dijet production in both pp and pA collisions and the theoretical framework used in this study. In the discussion about pp (Sec. II A) we focus on the dijet kinematics and the necessity to introduce the triple-differential cross section. In the subsection about pA (Sec. II B) we pay attention to the initial-state cold nuclear matter effects related to the nPDFs. In Sec. III we study three types of triple-differential cross sections and the corresponding nuclear modification factors R_{pA}. We establish links to compare the observable R_{pA} with the nPDF factors $r_i^A(x, Q^2)$. Possibilities to reveal the variation of $r_i^A(x, Q^2)$ with scale by using R_{pA} in different p_T regions are also discussed. We give a summary and discussion in Sec. IV.

II. DIJET PRODUCTION IN pp AND pA COLLISIONS

A. Dijet in pp collisions and kinematics

At partonic level the production of dijet in pp collisions is related to the processes of N-parton (quarks or gluons, $N \geq 2$) production initiated by partons a and b from the two colliding protons. In perturbative QCD, the cross section for the production of N partons in pp collisions can be generally expressed as the convolution of the parton distribution functions $f_i(x, Q^2)$ and the hard $2 \to N$ scattering cross section $d\hat{\sigma}_{ab}^{[2\to N]}$ [38]

$$\frac{d\sigma}{d\Phi_N} = \sum_{a,b} \int_0^1 dx_a \int_0^1 dx_b f_a(x_a, \mu_f^2) f_b(x_b, \mu_f^2) \times \frac{d\hat{\sigma}_{ab}^{[2\to N]}(x_a, x_b, \mu_r, \mu_f)}{d\Phi_N}, \quad (1)$$

where $\Phi_N \equiv \Phi_N(p_1, \ldots, p_N)$ represents the phase space of the final-state N partons, x_a (x_b) is the momentum fraction carried by the incoming parton from the forward- (backward-)going proton, and μ_f (μ_r) is the factorization (renormalization) scale. The right-hand side of Eq. (1) is summed over the flavors of partons a and b, essentially including quark-quark, quark-gluon, and gluon-gluon initial states.

At NLO in perturbative calculation, where only $2 \to 2$ and $2 \to 3$ partonic processes are involved, a dijet observable, such as an m-fold differential cross section $d\sigma / \prod_{j=1}^m dv_j$ defined with the dijet kinematic variables $V^{(m)} = \{v_1, \ldots, v_m\}$, can be calculated with [38]

$$\frac{d\sigma}{\prod_{j=1}^m dv_j} = \int d\Phi_2(p_1, p_2) \frac{d\sigma}{d\Phi_2} S_2(p_1, p_2) + \int d\Phi_3(p_1, p_2, p_3) \frac{d\sigma}{d\Phi_3} S_2(p_1, p_2, p_3). \quad (2)$$

Here all the constraints imposed on final state, including jet algorithm, are embodied in functions $S_N(p_1, \ldots, p_N)$, which should be properly defined to satisfy the infrared safe conditions [38].

Equations (1) and (2) link the measurable dijet cross section to the not directly measurable parton distribution

functions $f_i(x, Q^2)$, within the framework of factorization. Conventionally, to nicely disclose the x and Q^2 dependence of the PDFs at an observable level, one can establish a one-to-one correspondence between the values of $V^{(m)}$ and those of x and Q^2 in the leading-order (LO) approximation, by properly choosing the dijet variables $V^{(m)}$.

For instance, one applicable variable set to define a double-differential cross section may be $V^{(2)} = \{M_{JJ}, y_{\rm dijet}\}$ [41], with the squared invariant mass $M_{JJ}^2 \equiv (p_1 + p_2)^2$ and rapidity $y_{\rm dijet}$ of the jet pair. Note that a similar choice is usually used in DY measurements. With this choice, one can connect $V^{(m)}$ with $x_{a(b)}$ through the LO relation

$$x_{a(b)} = \frac{M_{JJ}}{\sqrt{s}} e^{\pm y_{\rm dijet}}, \tag{3}$$

which enables a kinematic scan of $x_{a(b)}$. Besides, one physical scale M_{JJ} is also well controlled. Unlike the DY process, where the typical hard scale is the invariant mass of the lepton pair, there is an additional physical scale in dijet production, i.e., the jet transverse momentum ($p_{T1} = p_{T2}$ at LO), which is not yet fully controlled with the above choice of $V^{(m)}$.

As a matter of fact, the number of independent kinematic variables of the dijet final state is 3 at LO [35]. Therefore, by defining a triple-differential cross section with $V^{(3)} = \{v_1, v_2, v_3\}$, one may simultaneously resolve $x_{a(b)}$ and the scales at which the parton distributions are probed. One straightforward example is to set $V^{(3)} = \{M_{JJ}, y_{\rm dijet}, p_{T,\rm avg}\}$, with $p_{T,\rm avg} = (p_{T1} + p_{T2})/2$. On the other hand, the high statistics at the LHC are sufficient for a precise measurement of the more differential observable [42].

In general, the established LO correspondence can be more or less broken once the higher-order corrections are considered. As a result, for a realistic observable, it is inevitable that the subprocesses associated with various values of x, Q^2 and i (flavor) jointly contribute to the measurement at a single set of $V^{(m)}$. A demonstration in a kinematic perspective is presented as follows.

For a process of N-parton production, one can infer the initial-state momentum fraction x_a (x_b) by summing the forward (backward) components of the light-cone momenta over all the N final-state partons as [35]

$$x_{a(b)} = \sum_{n=1}^{N} \frac{p_n^{\pm}}{\sqrt{s}} = \sum_{n=1}^{N} \frac{E_{Tn}}{\sqrt{s}} e^{\pm y_n}, \tag{4}$$

with the light cone component $p_n^{\pm} \equiv p_n^0 \pm p_n^3 = E_{Tn} e^{\pm y_n}$, transverse energy $E_{Tn} = (m^2 + p_{Tn}^2)^{1/2}$, and rapidity y_n of parton n. However, in an inclusive measurement of dijet, one can not fully deduce the values of x_a and x_b, since the final-state particles that lie outside the dijet cones are not restricted, which could happen at NLO and beyond. These issues also underlie the fact that the global QCD analysis for the PDFs is necessary and complicated.

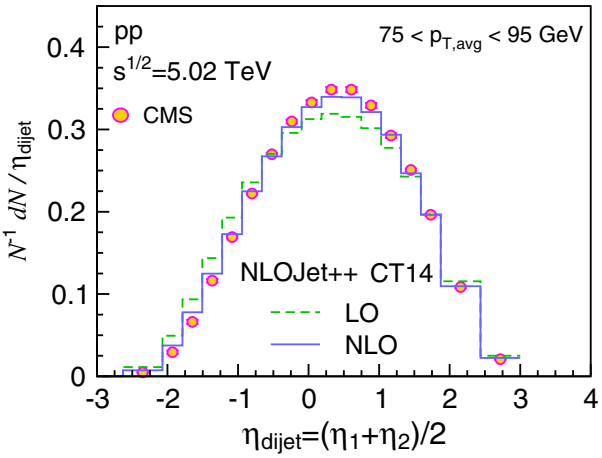

FIG. 1. Normalized dijet pseudorapidity distribution in pp collisions at $\sqrt{s} = 5.02$ TeV. Here $\eta_{\rm dijet}$ is defined in laboratory frame in pPb collisions, thus is related to that in center of mass frame as $\eta_{\rm dijet} = \eta_{\rm dijet}^{\rm cm} + 0.465$ [25]. Theoretical results are calculated at LO (dashed) and NLO (solid), with CT14 LO and NLO proton PDFs, respectively. Circle represents CMS data (vertical uncertainty bar is small) [25]. Jets are found by anti-k_T algorithm with cone size $R = 0.3$ and with rapidity cut $|y_{\rm lab}| < 3$. Averaged transverse momentum of dijet is restricted with $75 < p_{T,\rm avg} < 95$ GeV. Relative azimuthal angle of jet pair is restricted with $|\Delta\phi_{12}| > 2\pi/3$. Cuts imposed on transverse momenta of leading and subleading jets are $p_{T1} > 30$ GeV and $p_{T2} > 20$ GeV, respectively [25].

Nonetheless, since the LO processes may give a dominant contribution, one can still expect that the triple-differential dijet cross sections have a nice resolution power for the x and Q^2 dependence of PDFs, which is beneficial to the global analysis [42].

In this work, we will calculate the double- and triple-differential dijet cross sections to NLO in perturbative QCD by using the code NLOJet++ [36,37]. To test the numerical calculations, we first show in Fig. 1 the results for dijet pseudorapidity [$\eta_{\rm dijet} = (\eta_1 + \eta_2)/2$] distribution in pp collisions, which has been measured by the CMS Collaboration [25]. We find that the CMS data can be decently described to some extent by the NLO calculation (see a χ^2 analysis in Ref. [30]), in which the CT14 proton PDFs [43] are used and the factorization and renormalization scales are taken to be $\mu_0 = \mu_f = \mu_r = p_{T,\rm avg}$.

Since this $\eta_{\rm dijet}$ distribution is measured with the averaged transverse momentum of dijet $p_{T,\rm avg}$ being restricted, the normalized distribution $N^{-1}dN/d\eta_{\rm dijet}$ shown in Fig. 1 actually corresponds to the double-differential cross section $\sigma^{-1}d^2\sigma/d\eta_{\rm dijet}dp_{T,\rm avg}$ with $V^{(2)} = \{\eta_{\rm dijet}, p_{T,\rm avg}\}$. Note that, even at LO, neither the dijet invariant mass M_{JJ}

nor $x_{a(b)}$ are uniquely determined with a certain set of $\{\eta_{\text{dijet}}, p_{T,\text{avg}}\}$, while the ratio $x_a/x_b = e^{2\eta_{\text{dijet}}}$ is fixed. Overall, the averaged value of $x_{a(b)}$ will increase (decrease) with an increasing η_{dijet} [25]. We leave a further discussion to Sec. III.

B. Dijet in pA collisions and cold nuclear matter effects

In pA collisions, the differences between nuclear PDFs and free-nucleon PDFs may result in nuclear modifications on dijet cross section relative to that in pp collisions, which are also referred to as the initial-state cold nuclear matter (CNM) effects [44]. The nuclear correction on parton distribution is usually quantified with the ratio of the PDF in the bound nuclear proton to that in free proton as

$$r_i^A(x, Q^2) = \frac{f_i^{A,p}(x, Q^2)}{f_i^p(x, Q^2)}. \tag{5}$$

Generally, the nuclear correction factors $r_i^A(x, Q^2)$ are determined by the additional nonperturbative dynamics with the presence of nuclear environment, and they depend on the nuclear mass number A, parton flavor i, momentum fraction x and the resolution scale Q^2. Phenomenologically, the nuclear effects, i.e., $r_i^A(x, Q^2) \neq 1$, are conventionally classified, from small to large values of x, as the shadowing, antishadowing, EMC, and Fermi motion [3,5].

In this work, to include the initial-state CNM effects in pA collisions, we use four parametrization sets of nuclear PDFs, i.e., EPPS16 [17], nCTEQ15 [15], TUJU19 [18], and nIMParton16 [16] in the calculations. In Fig. 2 we plot the factors $r_i^A(x, Q^2)$ for gluon and (total) quark distributions in lead (^{208}Pb) nucleus from the four nPDF sets, at the scale $Q = 100$ GeV. Considerable differences among these nPDF sets can be observed, especially for gluon distribution. For some specific values of the variable x, some nPDFs give enhancements and others can give suppressions, which means the ranges of each kind of nuclear effect are not yet clear. These issues also motivate our study for a more delicate kinematic scan of the nPDFs in pA collisions. In this work, we will focus on how these differences are reflected in dijet observables. We hope our study is helpful for the future measurements to clarify the ranges of these nuclear effects.

In our calculations for dijet production, to unify the baseline pp results, we have used the factors $r_i^A(x, Q^2)$ from the four nPDF sets on top of the CT14 proton PDFs for pA collisions. We note that nCTEQ15, TUJU19, and nIMP16 nPDFs are extracted with their own proton PDFs other than CT14 (e.g., nCTEQ15 uses a variant of the CTEQ6M PDFs [15]), and we have neglected this difference since we only focus on the nuclear modifications in this work. In addition, because nIMP16 is obtained in a LO QCD analysis [16], we only do the LO calculation when using nIMP. The other three nPDF sets are used in NLO calculations. In this study, we have only considered the nuclear corrections on the leading-twist PDFs and not focused on the possible higher-twist nuclear effects [45,46]. Besides, since there has been no clear experimental evidence of the possible final-state jet quenching effects in pA collisions [47,48], we have only considered the initial-state CNM effects.

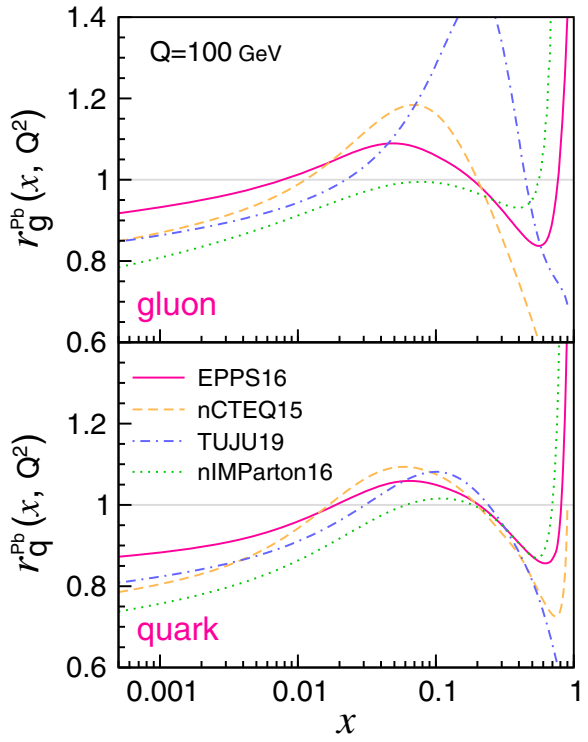

FIG. 2. Nuclear correction factors $r_i^{\text{Pb}}(x, Q^2)$ for gluon (top panel) and quark (bottom panel) distributions in lead nucleus from four nPDF sets, EPPS16, nCTEQ15, TUJU19, and nIMParton16 at $Q = 100$ GeV. Unless otherwise specified, the quark distribution mentioned in this paper means the total (or singlet) distribution for the active quark flavors defined as $f_{\text{quark}}(x, Q^2) \equiv \sum_i [q_i(x, Q^2) + \bar{q}_i(x, Q^2)]$, and according to Eq. (5) the factor $r_{\text{q(uark)}}^{\text{Pb}} = f_{\text{quark}}^{\text{Pb},p}/f_{\text{quark}}^p$.

As an example, we calculate the normalized η_{dijet} distribution in proton-lead (pPb) collisions, corresponding to that in pp collisions shown in Fig. 1, and plot the ratio of the results in pPb and pp collisions in Fig. 3, where the CMS data [25] are also shown for comparison. Differences among the predictions with four nPDF sets can be seen, and since the CMS measurement is very precise, the experimental uncertainties can be even smaller than the differences among various predictions in a wide range of η_{dijet}. The results with EPPS16 show a nice overall agreement with the data, except for that in forward region related to the shadowing at small x. This is consistent with the results in Ref. [25]. We also note that the EPPS reweighted with the CMS dijet data indeed suggests a stronger

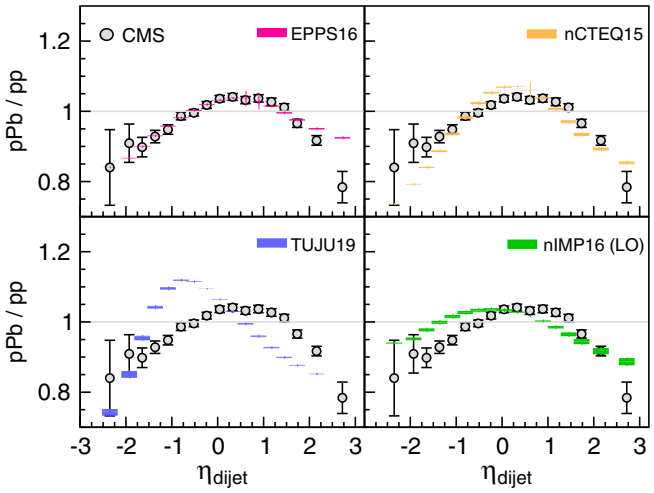

FIG. 3. Ratio of normalized dijet η_{dijet} distribution in pPb and pp collisions, corresponding to Fig. 1. Circle with vertical bar represents CMS data with uncertainty [25]. Colored lines represent theoretical predictions with four nPDFs sets, i.e., EPPS16, nCTEQ15, TUJU19, and nIMParton16, with bands corresponding to variations with factorization/renormalization scales $(\mu_0/2, \mu_0, 2\mu_0)$ in perturbative calculations. Results with nIMP16 are calculated at LO, while results with other three nPDF sets are calculated at NLO.

shadowing suppression in gluon distribution [30]. The results with nCTEQ15 can also well describe the data. However, the predictions with both TUJU19 and nIMP16 show deviations from the data to some extents. For example, in the region around $\eta_{\text{dijet}} \sim -1$, TUJU19 predicts a strong enhancement, which is not observed in the data. This enhancement is related to the strong gluon antishadowing effect as seen in Fig. 2 ($x \sim 0.2$). We note that TUJU19 also provides NNLO nPDFs, in which a weaker antishadowing effect is suggested [18].

It should be mentioned that the aim of this study is not to rule out any parameterized nPDFs, but to provide a more intuitive way for studying the differences among various nPDF sets and to facilitate more effective measurements in future. Thus, in the calculations, we only use the central values of the nPDFs without considering their uncertainties. In Fig. 3 (and also in following figures), the bands for the theoretical results correspond to the variations with factorization/renormalization scales $(\mu_0/2, \mu_0, 2\mu_0)$ in the perturbative calculations.

Due to the high accuracy, the CMS data have already provided a powerful constraint on the nPDFs, especially on nuclear gluon distribution [30]. However, the initial-state parton momentum fraction x is not fully controlled at LO (as discussed in Sec. II A) which results in the mixing of different nuclear effects in the observable. Next, we discuss the possibility to make further improvement on the observable level, i.e., to reduce the extent of the mixing by using triple-differential dijet cross section.

III. TRIPLE-DIFFERENTIAL DIJET CROSS SECTION AND NUCLEAR MODIFICATIONS IN PROTON-LEAD COLLISIONS

As is discussed in Sec. II A, a triple-differential dijet cross section provides a more direct resolution of the x and Q^2 dependence of the PDFs $f_i(x, Q^2)$. This idea has been applied to pp collisions to study the proton PDFs [35,39,42]. However, in pp collisions, even a triple-differential cross section can still involve two different momentum fractions, x_a and x_b, carried by the two initial partons [39]. Besides, to make a more adequate comparison with a measured cross section, the NNLO corrections may be needed in a theoretical prediction [39]. In contrast, in the study of nuclear modifications in pA collisions, these problems can be avoided to a large extent, and the triple-differential cross section has more advantages. On one hand, the parton incoming from the single nucleus target only involves one momentum fraction variable, whereas the parton from proton can be viewed as a probe. On the other hand, if we focus on the nuclear correction factors $r_i^A(x, Q^2)$ instead of the nPDFs themselves, both the theoretical and experimental uncertainties can be reduced effectively.

Concretely, one can study the conventional nuclear modification factor for such cross sections defined as the ratio of the cross sections in pA and pp collisions normalized by the nuclear mass number A [49]

$$R_{pA}(v_1, v_2, v_3) = \frac{1}{A}\frac{d\sigma^{pA}/dv_1dv_2dv_3}{d\sigma^{pp}/dv_1dv_2dv_3}. \tag{6}$$

This R_{pA} can be schematically expressed in LO approximation as [35]

$$R_{pA}(v_1, v_2, v_3) \approx \frac{\sum_{a,b} f_a^p(x_a, \mu^2) f_b^A(x_b, \mu^2) H_{ab}(v_1, v_2, v_3)}{\sum_{a,b} f_a^p(x_a, \mu^2) f_b^p(x_b, \mu^2) H_{ab}(v_1, v_2, v_3)}, \tag{7}$$

where f_b^A is the averaged per nucleon PDF in the nucleus, and H_{ab} represents the perturbatively calculable hard function. Apparently, this R_{pA} provides an intuitive insight into the nuclear correction factor $r_i^A(x, Q^2)$ defined in Eq. (5). Please note that, for a given set of $\{v_1, v_2, v_3\}$, the values of variables $x_{a(b)}$, M_{JJ}, and $p_{T,\text{avg}}$ are uniquely determined at LO.

Since the R_{pA} is defined as a ratio in Eq. (6), the total uncertainties in both theoretical and experimental sides can be reduced significantly. In theoretical calculations, the uncertainties (e.g., from proton PDFs and high-order corrections) of the numerator and denominator may cancel each other to some extents. Similarly, systematical uncertainties may be reduced effectively in experimental measurements. Next, we will study the $R_{p\text{Pb}}$ for several types of

triple-differential dijet cross sections in pPb collisions at the LHC.

A. Nuclear modifications on $d^3\sigma/dp_{T,\mathrm{avg}}dy_b dy^*$

We first study the nuclear modification on a triple-differential dijet cross section with $\{v_1, v_2, v_3\} = \{p_{T,\mathrm{avg}}, y_b, y^*\}$ that has been measured in pp collisions by CMS Collaboration [42]. Here y_b and y^* are defined with the rapidity of the two jets as $y_b = |y_1 + y_2|/2$ and $y^* = |y_1 - y_2|/2$. For convenience, we write the LO kinematic relations as [39]

$$x_a = \frac{M_{JJ}}{\sqrt{s}} e^{\pm y_b}, \qquad x_b = \frac{M_{JJ}}{\sqrt{s}} e^{\mp y_b},$$
$$\text{with} \quad M_{JJ} = 2p_{T,\mathrm{avg}} \cosh(y^*), \tag{8}$$

where the symbol $\pm(\mp)$ is owing to the definition of y_b as an absolute value. In Fig. 4, we plot the results for $d^3\sigma/dp_{T,\mathrm{avg}}dy_b dy^*$ against $p_{T,\mathrm{avg}}$ in pp collisions at $\sqrt{s} = 8$ TeV, with $y_b \in [0, 1]$ and $y^* \in [0, 1]$. The CMS data can be well described by the perturbative calculations, in which both the factorization and renormalization scales are taken to be $\mu_0 = p_{T1}e^{0.3y^*}$ [42], which is a compromise between p_T and $M_{JJ}/2$ as first investigated in Ref. [33]. The NNLO corrections have been found to give ~10% or more enhancements in Ref. [39]. Next, we apply this cross section in pPb collisions in the same kinematic regions.

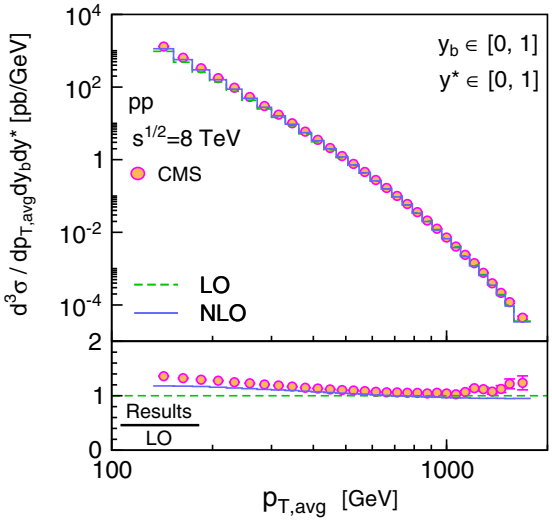

FIG. 4. Triple-differential cross section $d^3\sigma/dp_{T,\mathrm{avg}}dy_b dy^*$ in pp collisions at $\sqrt{s} = 8$ TeV with $y_b \in [0, 1]$ and $y^* \in [0, 1]$. Theoretical results at LO (dashed) and NLO (solid) are compared to CMS data represented with circles (vertical uncertainty bars are small) [42]. Jets are found by anti-k_T algorithm with cone size $R = 0.7$ and with rapidity cut $|y| < 5$. Additional cuts imposed on transverse momentum and rapidity of leading jet are $p_{T1} > 50$ GeV and $|y_1| < 3$, respectively [42]. Ratios between shown results and LO ones are plotted at bottom as a reference.

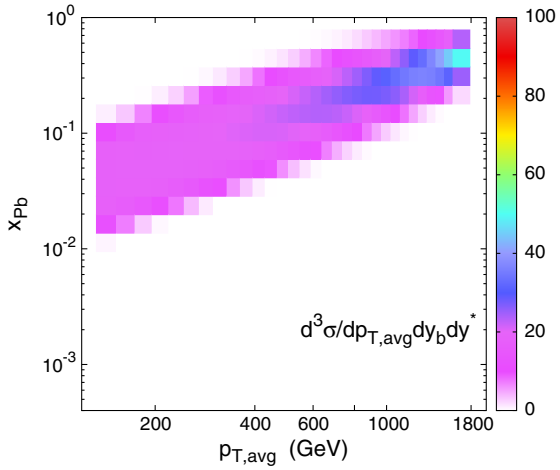

FIG. 5. Correlations between each $p_{T,\mathrm{avg}}$ bin and momentum fraction x_{Pb} carried by initial nuclear parton for triple-differential dijet cross section $d^3\sigma/dp_{T,\mathrm{avg}}dy_b dy^*$. For each $p_{T,\mathrm{avg}}$ bin, total contributions from various values of x_{Pb} in the considered region $x_{\mathrm{Pb}} \in [5 \times 10^{-4}, 0.78]$ are normalized to be unity (100%). Values of correlations are represented with rainbow colors (0–100%). They are calculated by counting cross sections in $p_{T,\mathrm{avg}}$ and x_b bins in pp collisions (without nuclear effects) at LO.

To visualize the capability of this $d^3\sigma/dp_{T,\mathrm{avg}}dy_b dy^*$ to resolve the momentum fraction x_{Pb} of the initial parton from lead nucleus, we illustrate in Fig. 5 the correlations between each $p_{T,\mathrm{avg}}$ bin and x_{Pb}, calculated at LO and represented with the rainbow colors. It is noted that, for a certain $p_{T,\mathrm{avg}}$ bin, the x_{Pb} can spread over an order of magnitude due to the nonvanishing bin sizes of $\Delta p_{T,\mathrm{avg}}$, Δy_b, and Δy^* in the measurement. Nevertheless, an overall linear relation is observed as expected from Eq. (8).

The nuclear modification factors $R_{p\mathrm{Pb}}$ for pPb collisions are calculated with three nPDFs sets (EPPS16, nCTEQ15 and TUJU19) at NLO and with nIMP16 at LO, and are shown in the top panel of Fig. 6. Differences among the four predictions as well as the $p_{T,\mathrm{avg}}$ dependence of the results can be seen. Since the underlying x_{Pb} is around 0.1 as seen in Fig. 5—which is near the antishadowing region—we can see the enhancements predicted by several nPDF sets. Suppressions at large $p_{T,\mathrm{avg}}$ which correspond to the EMC region can also be observed. Currently, there has been no measurement of the triple-differential cross section in pPb collisions. To roughly estimate the constraining power of the future measurement, we show the relative statistical uncertainties in the CMS pp data [42] in the bottom panel of Fig. 6 for comparison. We find in a wide range of $p_{T,\mathrm{avg}}$, the relative uncertainties are much smaller than the differences among the nuclear modifications by various nPDFs, indicating a strong constraint on nPDFs. We also see that the uncertainties in high-$p_{T,\mathrm{avg}}$ region are too large to distinguish the EMC effects, related to the rapidly decreasing dijet yields with increasing $p_{T,\mathrm{avg}}$.

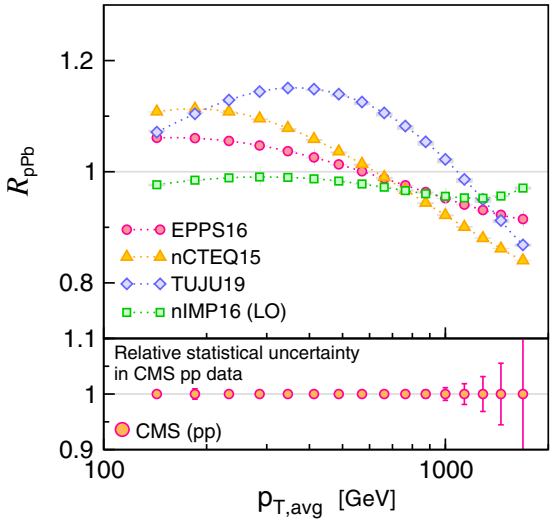

FIG. 6. Top panel: nuclear modification factor R_{pPb} corresponding to result in Fig. 4. Bottom panel: relative statistical uncertainties in CMS pp data in Fig. 4. R_{pPb} predicted by nIMP is calculated at LO, and those by other three nPDF sets are calculated at NLO. Gray bands (very thin) on R_{pPb} results correspond to variations with factorization/renormalization scales $(\mu_0/2, \mu_0, 2\mu_0)$. Note that vertical axes in both two panels are set in same scale to make a direct comparison.

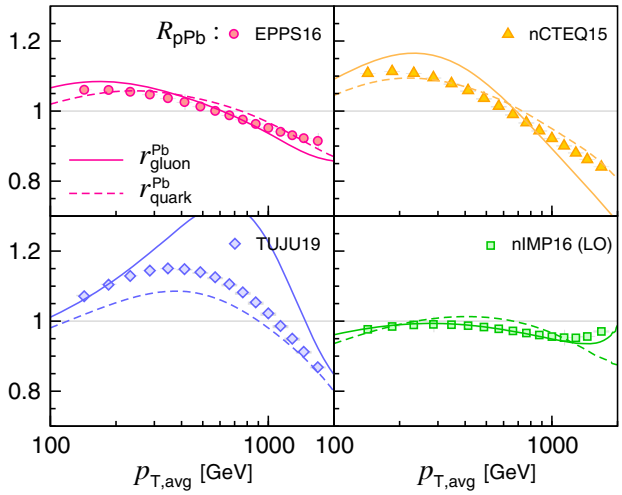

FIG. 7. Comparison between R_{pPb} (symbols) predicted by each nPDF set and its underlying nuclear corrections $r_i^{Pb}(x_{Pb}, Q^2)$ on gluon (solid) and total quark (dashed) distributions, corresponding to Fig. 6. Both R_{pPb} and r_i^{Pb} are shown as functions of $p_{T,avg}$. For plotting r_i^{Pb}, LO relation between x_{Pb} and $p_{T,avg}$ in Eq. (8) is used with $y_b = 0$ and $y^* = 0$ being set, and scale in $r_i^{Pb}(x_{Pb}, Q^2)$ is taken to be $Q = p_{T,avg}e^{0.3y^*}$.

Since we focus on the advantage of the triple-differential cross section on disclosing the underlying nuclear correction factor $r_i^A(x, Q^2)$ [as demonstrated with Eq. (7)], here we make a comparison between the observable R_{pPb} and the nPDF factor r_i^{Pb} in Fig. 7. Please note that the factors r_i^{Pb} for gluon and quark distributions are plotted against $p_{T,avg}$ instead of x_{Pb}. To make this variable substitution, we have used the LO relation in Eq. (8) as $x_{Pb} = 2p_{T,avg}/\sqrt{s}$ with y_b and y^* taken to be 0. Meanwhile, the scale Q in $r_i^{Pb}(x, Q^2)$ is taken to be $Q = p_{T,avg}e^{0.3y^*}$ when it is plotted. We find that the R_{pPb} predicted by various nPDF sets are comparable with their own r_i^{Pb}, even though three sets of them (EPPS16, nCTEQ15, and TUJU19) are calculated at NLO where the linear relation may be somewhat broken. The comparison in Fig. 7 provides an intuitive way to understand the different R_{pPb} given by different nPDF sets. For example, we can see that the strong antishadowing in gluon distribution of TUJU19 significantly enhances the predicted R_{pPb}.

The correspondence between $p_{T,avg}$ and x_{Pb} plays an important role in this comparison. However, in a single $p_{T,avg}$ bin as in the CMS measurement, the mixing of the contributions from various values of x_{Pb} is too strong to allow a more delicate kinematic scan, as shown in Fig. 5. This mixing could be lessened by narrowing the bin sizes in the measurement of $d\sigma/dp_{T,avg}dy_b dy^*$, at the cost of statistical accuracy. On the other hand, there are different ways to define the triple-differential cross sections, which will be discussed in the following subsections.

B. Nuclear modifications on $d^3\sigma/dX_B dX_A dy^*$

Another choice of dijet variables to define a triple-differential cross section is $\{v_1, v_2, v_3\} = \{X_A, X_B, y^*\}$, proposed by Ellis and Soper for the study of parton distributions in $pp(\bar{p})$ collisions [35], with two new variables defined as

$$X_A = \sum_{n\in\text{dijet}} \frac{E_{Tn}}{\sqrt{s}} e^{+y_n}, \qquad X_B = \sum_{n\in\text{dijet}} \frac{E_{Tn}}{\sqrt{s}} e^{-y_n}, \quad (9)$$

which are similar as the expression of $x_{a(b)}$ in Eq. (4). Here the summation is performed over all the particles inside the dijet cones. Apparently, the LO relation $X_{A(B)} = x_{a(b)}$ provides a direct connection to the initial momentum fractions. At NLO, it still holds for the case that all the partons fall into the dijet cones, and becomes $X_{A(B)} \leq x_{a(b)}$ only when there is one parton lying outside. In Ref. [35], it is shown that the NLO corrections on the cross section $d^3\sigma/dX_B dX_A dy^*$ can be small.

We first calculate the cross sections in pp collisions at $\sqrt{s} = 8.16$ TeV and show the results as functions of X_B in Fig. 8, where the left and right panels correspond to the regions $X_A \sim 0.1$ and $X_A \sim 0.01$, respectively. By restricting X_A, one actually controls the x_a carried by the forward-going initial parton (the "probe" of nPDFs in pA). We find that, for $X_A \sim 0.1$, dijet production covers a wide range of X_B (from 10^{-3} to 0.8), where the LO and NLO results are close to each other. We also check the dijet yields in each $\Delta X_B \Delta X_A \Delta y^*$ bin (integrated cross section), and find the

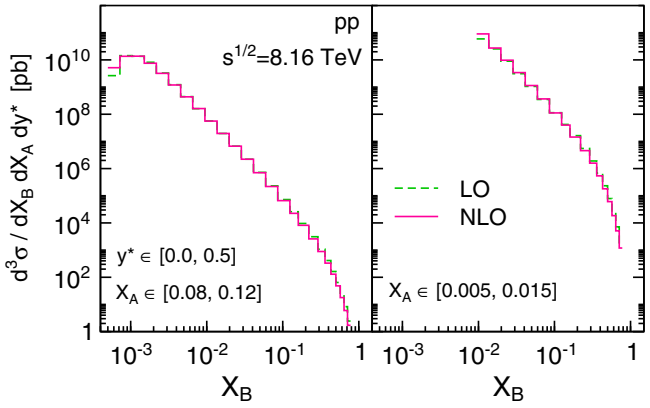

FIG. 8. Triple-differential cross section $d^3\sigma/dX_B dX_A dy^*$ versus X_B in pp collisions at $\sqrt{s} = 8.16$ TeV. Left and right panels correspond to two regions of X_A, $X_A \in [0.08, 0.12]$ and $X_A \in [0.005, 0.015]$, respectively. The third variable y^* is restricted with $y^* \in [0, 0.5]$. Theoretical results are calculated at LO (dashed) and NLO (solid). Jets are found by anti-k_T algorithm with cone size $R = 0.7$ and with rapidity cut $|y| < 2.5$. Relative azimuthal angle of jet pair is restricted with $|\Delta\phi_{12}| > 2\pi/3$. Cuts imposed on transverse momenta of leading and subleading jets are $p_{T1} > 30$ GeV and $p_{T2} > 20$ GeV, respectively [25].

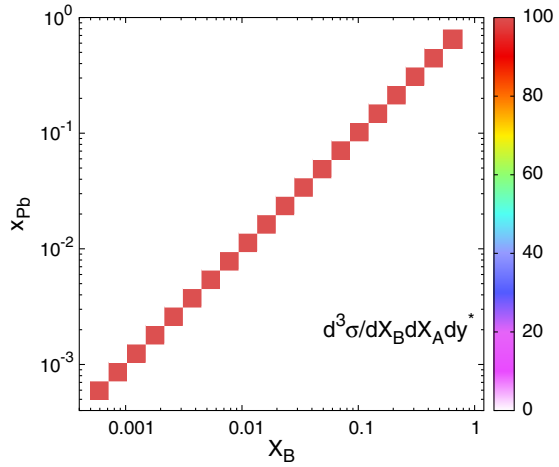

FIG. 9. Similar as Fig. 5, but for correlations between X_B and $x_{\rm Pb}$ in triple-differential cross section $d^3\sigma/dX_B dX_A dy^*$, corresponding to left panel of Fig. 8. Bin sizes for X_B and $x_{\rm Pb}$ are set to be same.

yields here are similar as the those in Fig. 4, and can be even larger for high-x region. By lowering X_A to be around 0.01, as shown in the right panel in Fig. 8, we find the dijet yields in large-X_B regoin can increase approximately by two orders of magnitude, indicating a higher statistical accuracy for probing the large-x parton distributions.[1] Since we have limited the jet transverse momenta as $p_{T1} > 30$ GeV and $p_{T2} > 20$ GeV [25], the X_B is unlikely to be very small for a lower X_A.

In our calculations, the factorization/renormalization scale is taken to be $\mu_0 = \sqrt{X_A X_B s}/[4\cosh(0.7y^*)]$ [35]. Besides, the relative azimuthal angle of the two jets is restricted as $|\Delta\phi_{12}| > 2\pi/3$ [25], through which the jet pair is selected to be nearly back to back. This constraint is imposed to reduce the contributions of the case that partons lie outside the dijet cones (but become useless for the partons colinearly emitted by initial partons).

Next, let us discuss for the pPb collisions. The correlations between X_B and $x_{\rm Pb}$ at LO are plotted in Fig. 9, and a perfect linear correspondence can be observed as expected; importantly, it does not depend on the bin sizes of ΔX_A and Δy^*. This high resolution may allow a more detailed kinematic scan of the nuclear PDF factors $r_i^{\rm Pb}(x_{\rm Pb}, Q^2)$ (see Appendix A for more discussions on the resolution power at NLO).

The nuclear modification factors $R_{p\rm Pb}$ on the triple-differential cross sections $d^3\sigma/dX_B dX_A dy^*$ are calculated with four nPDF sets (EPPS16, nCTEQ15, and TUJU19 at NLO and nIMP16 at LO), and shown in top panels (A0) and (B0) of Fig. 10 for $X_A \sim 0.1$ and $X_A \sim 0.01$, respectively. A clear X_B dependence is observed, and the results here are similar as the $r_i^{\rm Pb}(x_{\rm Pb}, Q^2)$ shown in Fig. 2. With the LO approximation $X_B = x_{\rm Pb}$ in mind, we can roughly identify the shadowing, antishadowing, EMC, and Fermi motion effects in the observable $R_{p\rm Pb}$.

The results in panels (A0) and (B0) with four nPDF sets are then separately shown in panels (A1-4) and (B1-4), and are compared to their corresponding nPDF factors $r_i^{\rm Pb}(x_{\rm Pb}, Q^2)$ for gluon and quark distributions. We see a very nice agreement between the $R_{p\rm Pb}$ and $r_i^{\rm Pb}$. In particular, the $R_{p\rm Pb}$ approaches to $r_{\rm gluon}^{\rm Pb}$ for gluon distribution at small X_B ($\lesssim 0.01$), and is close to $r_{\rm quark}^{\rm Pb}$ for quark distribution at large X_B ($\gtrsim 0.3$). This is reasonable, since the dijet production at small X_B is dominated by the nuclear gluon initiated processes, whereas at large X_B the nuclear (valence) quarks play a dominant role. We also see that, in the intermediate X_B region, $R_{p\rm Pb}$ results from the interplay of $r_{\rm gluon}^{\rm Pb}$ and $r_{\rm quark}^{\rm Pb}$. In this sense, the $R_{p\rm Pb}(X_B)$ on the observable level can serve as an image of the nuclear modifications on parton distributions, i.e., the $r_i^{\rm Pb}$ factors, owing to the high resolution power for $x_{\rm Pb}$ of the cross section $d^3\sigma/dX_B dX_A dy^*$.

On the other hand, we note that the physical scales will vary with the X_B in this cross section, which means the nuclear modifications at different values of X_B are probed at different scales. For example, at LO one has

[1]It is also noteworthy that, in pA collisions, the measurements of such cross sections could be extended to the region $X_B > 1$ to offer a relatively direct probe of the nPDFs for $x > 1$, and to gain insight into this currently poorly understood kinematic region, where the nPDFs are possibly nonzero due to the (Fermi) motion of nucleons inside the nuclei (see Refs. [50,51] for recent experimental and theoretical developments). The authors appreciate the Referee for bringing to their attention this point.

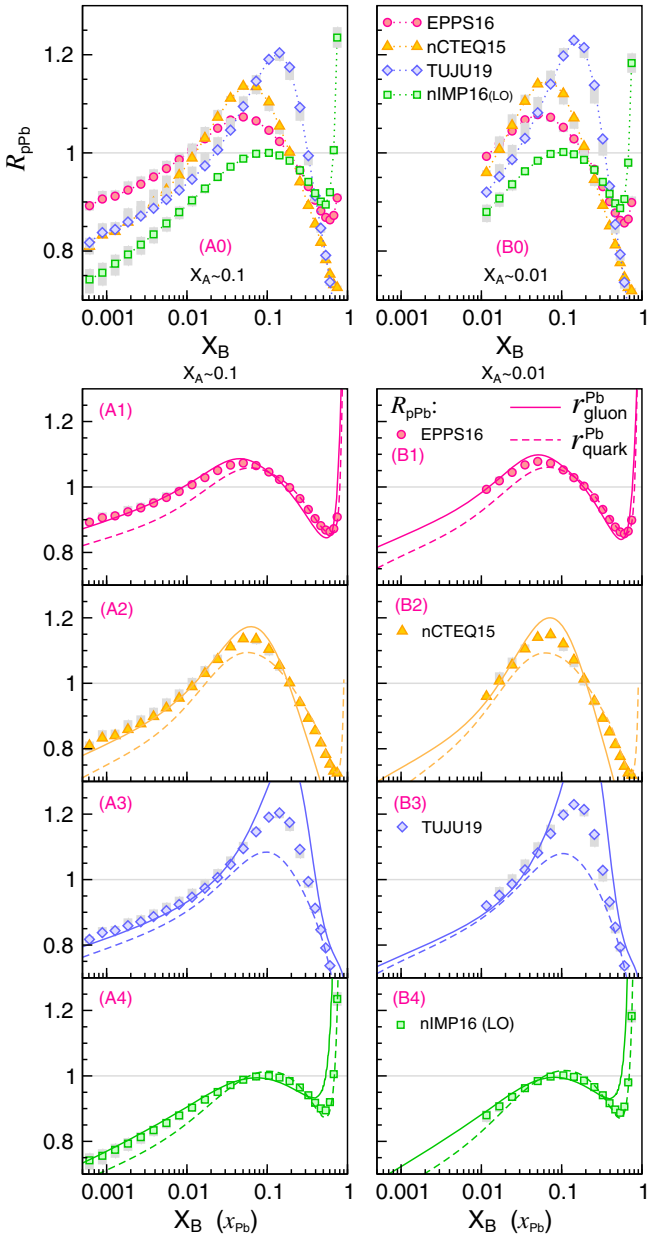

FIG. 10. Top panels (A0) and (B0): nuclear modification factors $R_{p\mathrm{Pb}}$ for $X_A \sim 0.1$ and $X_A \sim 0.01$ corresponding to Fig. 8, predicted by four nPDF sets and plotted with symbols plus dotted curves. Results of $R_{p\mathrm{Pb}}$ in panels (A0) and (B0) are separately shown in (A1-4) and (B1-4) with symbols, and compared with corresponding nPDF factors $r_i^{\mathrm{Pb}}(x_{\mathrm{Pb}}, Q^2)$ for gluon (solid) and total quark (dashed) distributions. One can note LO approximation $X_B = x_{\mathrm{Pb}}$ in this comparison. When plotting $r_i^{\mathrm{Pb}}(x_{\mathrm{Pb}}, Q^2)$, we have set $Q = \sqrt{X_A X_B s}/[4\cosh(0.7y^*)]$ with $X_A = 0.1(0.01)$ and $y^* = 0$. Gray bands on $R_{p\mathrm{Pb}}$ results correspond to variations with factorization/renormalization scales $(\mu_0/2, \mu_0, 2\mu_0)$.

$$M_{JJ} = \sqrt{X_A X_B s}, \qquad p_T = \sqrt{X_A X_B s}/[2\cosh(y^*)]. \quad (10)$$

For given values of X_A and y^*, both M_{JJ} and p_T increase with increasing X_B. (Note the choice of the factorization scale μ_0 in our calculation is a compromise between $M_{JJ}/4$ and $p_T/2$ [33]). As a matter of fact, if the values of both M_{JJ} and p_T are fixed, the only remaining degree of freedom of dijet kinematics at LO is the rapidity of dijet. Next, we study the dijet rapidity related triple-differential cross section, in which the physical scales do not vary.

C. Nuclear modifications on $d^3\sigma/dy_{\mathrm{dijet}}dE_T^{JJ}dp_{T,\mathrm{avg}}$ and $d^3\sigma/dX_B dE_T^{JJ}dp_{T,\mathrm{avg}}$

A triple-differential cross section can also be defined with the rapidity of dijet. Actually we have shown the dijet pseudo-rapidity distribution as measured by CMS in Sec. II A–II B (see Figs. 1 and 3). As has been discussed, the measured distribution is related to the double-differential cross section $d^2\sigma/d\eta_{\mathrm{dijet}}dp_{T,\mathrm{avg}}$, in which neither $x_{a(b)}$ nor M_{JJ} are fully controlled at a given set of $\{\eta_{\mathrm{dijet}}, p_{T,\mathrm{avg}}\}$. It can be improved by measuring a triple-differential one with $V^{(3)} = \{\eta_{\mathrm{dijet}}, M_{JJ}, p_{T,\mathrm{avg}}\}$. Nevertheless, here we note the kinematic relation

$$X_B = \frac{1}{\sqrt{s}} E_T^{JJ} \exp(-y_{\mathrm{dijet}}), \quad (11)$$

where X_B is defined in Eq. (9), E_T^{JJ} and y_{dijet} are transverse energy and rapidity of dijet defined as

$$E_T^{JJ} = \sqrt{M_{JJ}^2 + (\vec{p}_{T1} + \vec{p}_{T2})^2},$$
$$y_{\mathrm{dijet}} = \frac{1}{2}\ln\frac{E^{\mathrm{dijet}} + p_z^{\mathrm{dijet}}}{E^{\mathrm{dijet}} - p_z^{\mathrm{dijet}}}. \quad (12)$$

Since Eq. (11) holds for all orders in perturbative calculations, we defined an alternative dijet rapidity related cross section binned with $V^{(3)} = \{y_{\mathrm{dijet}}, E_T^{JJ}, p_{T,\mathrm{avg}}\}$, which has a more close connection to the variable X_B. At LO, this choice is equivalent to the $V^{(3)} = \{\eta_{\mathrm{dijet}}, M_{JJ}, p_{T,\mathrm{avg}}\}$, by noting that $E_T^{JJ} = M_{JJ}$ and $y_{\mathrm{dijet}} = \eta_{\mathrm{dijet}}$. Differences between the two choices only come from the high-order contributions.

To show the abilities of the observables to resolve x_{Pb} in pPb collisions, in Fig. 11, we compare the correlations between η_{dijet} and x_{Pb} in the double-differential cross section with $V^{(2)} = \{\eta_{\mathrm{dijet}}, p_{T,\mathrm{avg}}\}$, to those between y_{dijet} and x_{Pb} in the newly defined triple-differential one with $V^{(3)} = \{y_{\mathrm{dijet}}, E_T^{JJ}, p_{T,\mathrm{avg}}\}$. For the double-differential one, we observe a roughly linear correspondence between η_{dijet} and $\log x_{\mathrm{Pb}}$ resulting from $\eta_{\mathrm{dijet}} = \frac{1}{2}(\ln x_a - \ln x_{\mathrm{Pb}})$ at LO. However, it is smeared due to the remaining degree of freedom, e.g., x_a is not fixed. In contrast, we see a clear linear correlation in the triple-differential one, indicating a better resolution of x_{Pb}. Here the correlations between y_{dijet} and x_{Pb} are not exactly 100%, because the bin sizes of them are not fully matched, e.g., the $\log x_{\mathrm{Pb}}$ bins are equidistant

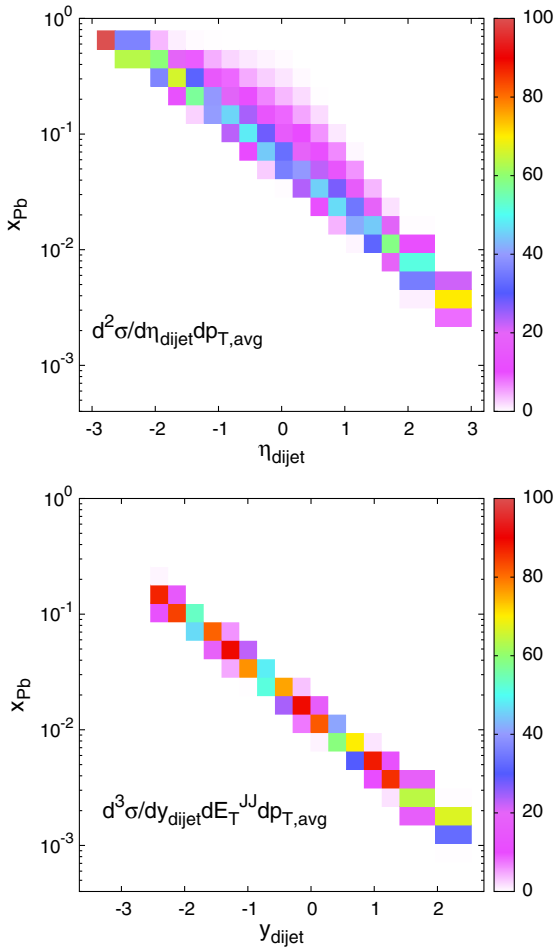

FIG. 11. Top panel: correlations between each $\eta_{\rm dijet}$ bin and $x_{\rm Pb}$ in double-differential cross section $d^2\sigma/d\eta_{\rm dijet}dp_{T,\rm avg}$ corresponding to CMS measurement in Figs. 1 and 3. Bottom panel: correlations between each $y_{\rm dijet}$ bin and $x_{\rm Pb}$ in triple-differential cross section $d^3\sigma/dy_{\rm dijet}dE_T^{JJ}dp_{T,\rm avg}$ corresponding to first panel in Fig. 12. Bin sizes for $\eta_{\rm dijet}$ and $y_{\rm dijet}$ are set to be same. See also caption of Fig. 5 for more details of calculations.

whereas the $y_{\rm dijet}$ are set to be the same as the $\eta_{\rm dijet}$ in CMS measurement, and also because the bin sizes of ΔE_T^{JJ} and $\Delta p_{T,\rm avg}$ are finite.

In the left-hand side panel of Fig. 12, we show the cross sections $d^3\sigma/dy_{\rm dijet}dE_T^{JJ}dp_{T,\rm avg}$ versus $y_{\rm dijet}$ in pp collisions at $\sqrt{s} = 5.02$ TeV, calculated at LO and NLO for three kinematic regions distinguished with the $\{p_{T,\rm avg}, E_T^{JJ}\}$ values. Please note that, for two jets with equal rapidity, one has $E_T^{JJ} = 2p_{T,\rm avg}$ at LO. Thus the top and middle plots correspond to the case that $y_1 \approx y_2$, on which a cut $|y_{1,2}| < 2.5$ is imposed. The bottom one corresponds to the case that two jets have a large rapidity difference ($|y_1 - y_2| \sim 4.5$ estimated with $E_T^{JJ}/2p_{T,\rm avg} = \cosh y^*$), thus a wider jet rapidity range $|y_{1,2}| < 4.5$ is considered. Besides, since the middle and bottom plots share a same E_T^{JJ} bin, they actually probe in the same $x_{\rm Pb}$ range, but with different $p_{T,\rm avg}$. In Fig. 12, we can also see that the NLO calculations give somewhat smaller cross sections than the LO ones. The factorzation/renormalization scale in the calculations is taken to be $\mu_0 = E_T^{JJ}/[4\cosh(0.7y^*)]$ [33], which is a compromise between $M_{JJ}/4$ and $p_T/2$ in LO kinematics.

Utilizing the correspondence between $y_{\rm dijet}$ and X_B in Eq. (11), one can easily transform the dijet variable $V^{(3)}$ from $\{y_{\rm dijet}, E_T^{JJ}, p_{T,\rm avg}\}$ to $\{X_B, E_T^{JJ}, p_{T,\rm avg}\}$. The transformed cross sections as functions of X_B, are plotted in the right-hand-side panel of Fig. 12. Since the top plot is calculated for a lower E_T^{JJ}, we can see that the dijets are produced in a smaller X_B region, compared to the middle and bottom ones. It is noteworthy that the LO correlations between X_B and $x_{\rm Pb}$ in pPb collisions should be the same as shown in Fig. 9, i.e., a one to one linear correspondence (independent of the bin sizes of ΔE_T^{JJ} and $\Delta p_{T,\rm avg}$).

The nuclear modification factors $R_{p\rm Pb}$ of the cross sections $d^3\sigma/dX_B dE_T^{JJ} dp_{T,\rm avg}$, corresponding to the results in Fig. 12, are calculated at NLO with several nPDF sets (except for nIMP16 at LO), and shown in panels (A0), (B0), and (C0) of Fig. 13. The results are very similar as those in Fig. 10. These $R_{p\rm Pb}$ predicted by four nPDF sets are then separately shown in panels (A1-4), (B1-4), and (C1-4), and are compared to their corresponding nPDF factors $r_i^{\rm Pb}(x_{\rm Pb}, Q^2)$ for gluon and quark distributions. By noting the LO approximation $X_B = x_{\rm Pb}$, we see again that the $R_{p\rm Pb}(X_B)$ results provide overall nice images of the $r_i^{\rm Pb}(x_{\rm Pb})$. With the increasing X_B, we can observe the transition from gluon-dominated to quark-dominated regions. In particular, considering that the physical scales are well controlled, we have plotted the $r_i^{\rm Pb}(x_{\rm Pb}, Q^2)$ in Fig. 13 at fixed values of Q^2, not like the Q^2 increasing with X_B in Fig. 10.

In panels (A1-3) of Fig. 13, we can see that the $R_{p\rm Pb}$ at small values of X_B (shadowing region) are slightly higher than the $r_{\rm gluon}^{\rm Pb}$ for gluon. This deviation may be partly attributed to the NLO process that a parton is co-linearly emitted by the initial nuclear parton. In this case, $X_B < x_{\rm Pb}$, which means the nuclear correction from a larger value of $x_{\rm Pb}$, e.g., in antishadowing region, may enter the $R_{p\rm Pb}$. As is expected, this effect is not observed in the nIMP16 results at LO shown in panel (A4). In panels (B1-4) and (C1-4), this effect is seen to be weaker. Please note that the values of the physical scales, $E_T^{JJ}(M_{JJ})$ and $p_{T,\rm avg}$, in these panels are larger than those in (A1-4). At a higher probing scale, the nuclear partons tend to carry smaller momentum fraction x and the contributions from the initial-state co-linear emission could be suppressed.

Since the $R_{p\rm Pb}(X_B)$ reflects the $r_i^{\rm Pb}(x_{\rm Pb}, Q^2)$ well at a certain value of Q^2, it raises an interesting question as to whether the $R_{p\rm Pb}(X_B)$ measured at different $p_{T,\rm avg}$ values can shed light on the variation of $r_i^{\rm Pb}(x_{\rm Pb}, Q^2)$ with Q^2.

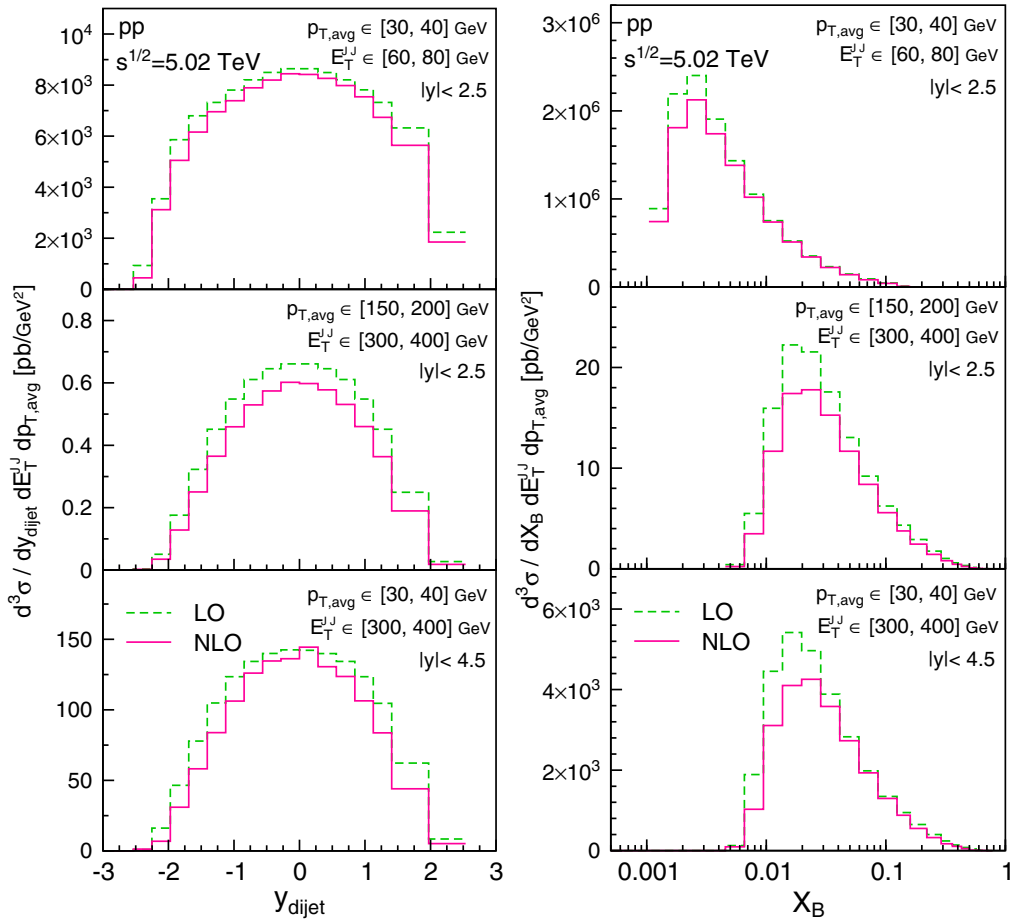

FIG. 12. Left panel: triple-differential dijet cross sections $d^3\sigma/dy_{\rm dijet}dE_T^{JJ}dp_{T,\rm avg}$ in pp collisions at $\sqrt{s} = 5.02$ TeV calculated at LO (dashed) and NLO (solid). Results are calculated for three $\{p_{T,\rm avg}, E_T^{JJ}\}$ regions and shown in top, middle, and bottom plots, respectively (see annotations in each plot for details). Right panel: similar as left one, but for $d^3\sigma/dX_B dE_T^{JJ} dp_{T,\rm avg}$. Kinematic restrictions for left and right plots are set to be same. Jets are found by anti-k_T algorithm with cone size $R = 0.7$. Relative azimuthal angle of jet pair is restricted with $|\Delta\phi_{12}| > 2\pi/3$. Cuts imposed on transverse momenta of leading and subleading jets are $p_{T1} > 30$ GeV and $p_{T2} > 20$ GeV, respectively [25].

A straightforward test can be made by utilizing the results in panels (B0) and (C0) of Fig. 13, which are in the same X_B range but correspond to two different $p_{T,\rm avg}$ regions, respectively. The ratios of the $R_{p\rm Pb}$ in the higher $p_{T,\rm avg}$ region (∼150 GeV) to those at the lower $p_{T,\rm avg}$ (∼30 GeV) are calculated and shown in panel (A) of Fig. 14. We find the $R_{p\rm Pb}$ given by four nPDF sets exhibit different variations with $p_{T,\rm avg}$. To further understand these distinctions, we plot in panels (B) and (C) the ratios of $r_i^{\rm Pb}(x_{\rm Pb}, Q^2)$ at $Q = 75$ GeV to those at $Q = 15$ GeV (simply taken to be $p_{T,\rm avg}/2$, neglecting the impact from E_T^{JJ}) for gluon and quark distributions, respectively. We observe that, for quark distribution, the variations of the $r_{\rm quark}^{\rm Pb}$ from the four nPDF sets have small distinctions. In contrast, for gluon distribution, significant differences among the results can be observed, which are similar as the differences seen in the variations of $R_{p\rm Pb}$ with $p_{T,\rm avg}$.

These results are somehow in accordance with the theoretical expectation from the collinear factorization of perturbative QCD [52]. Here, the dependence of $r_i^{\rm Pb}(x_{\rm Pb}, Q^2)$ on Q^2 results from the separate QCD evolutions of the nuclear PDFs (i.e., EPPS16, nCTEQ15, TUJU19, and nIMP16) and free-nucleon PDFs governed by the Dokshitzer-Gribov-Lipatov-Altarelli-Parisi (DGLAP) equations. It reflects the fact that at different resolution scales the nuclear modifications on partonic structures can be different in general (see Fig. 16 in Appendix B). The results in Fig. 14 indicate that the variations of the measured $R_{p\rm Pb}(X_B)$, at different kinematic energy scales of the hard scattering (related to $p_{T,\rm avg}$), is correlated to the underlying energy-scale dependence of nuclear modifications to some extent. In the context of QCD factorization [52], this is related to the feature that the renormalization group equation of the hard scattering cross section H_{ab}, which involves the

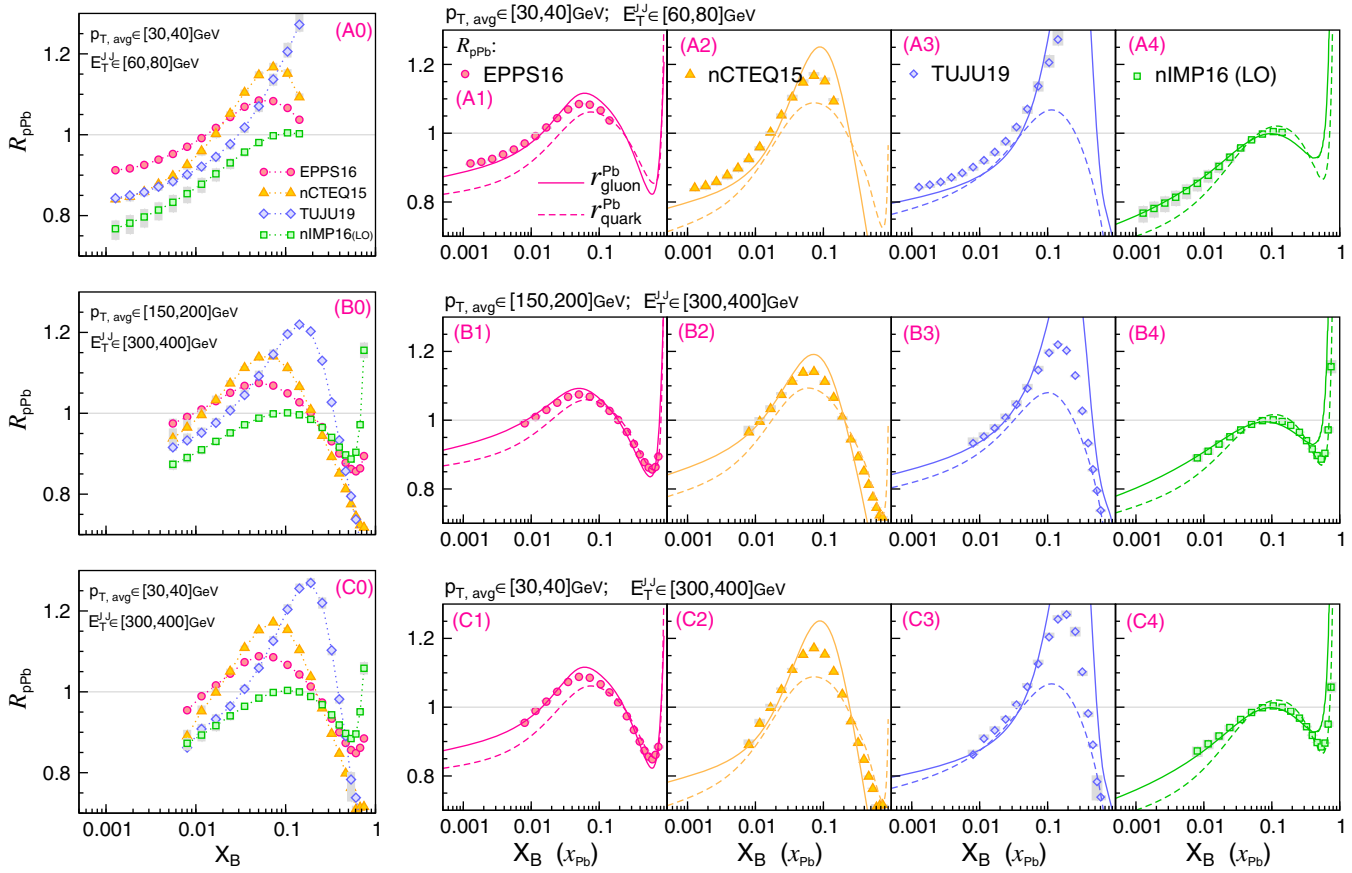

FIG. 13. Left panels (A0), (B0), and (C0) show nuclear modification factors $R_{p\mathrm{Pb}}$ of cross sections $d^3\sigma/dX_B dE_T^{JJ} dp_{T,\mathrm{avg}}$, corresponding to Fig. 12, predicted by four nPDF sets and plotted with symbols plus dotted curves. Results of $R_{p\mathrm{Pb}}$ in panels (A0), (B0), and (C0) are separately shown in (A1-4), (B1-4), and (C1-4) with symbols, and compared with corresponding nPDF factors $r_i^{\mathrm{Pb}}(x_{\mathrm{Pb}}, Q^2)$ for gluon (solid) and total quark (dashed) distributions. One can note LO approximation $X_B = x_{\mathrm{Pb}}$ in this comparison. When plotting $r_i^{\mathrm{Pb}}(x_{\mathrm{Pb}}, Q^2)$, we have set $Q = p_{T,\mathrm{avg}}/2$ (15, 75, and 15 GeV for three regions). Another choice $Q = E_T^{JJ}/[4\cosh(0.7y^*)]$ (15, 75, and 30 GeV for three regions) is also tested but not shown, with which a slightly better agreement between $R_{p\mathrm{Pb}}$ and r_i^{Pb} in third region is found. Gray bands on $R_{p\mathrm{Pb}}$ results correspond to variations with factorization/renormalization scales $(\mu_0/2, \mu_0, 2\mu_0)$, which are seen to be small.

kinematic energy scale, shares the same evolution kernels as in the DGLAP equation for PDFs.

Relevant to this feature, we have also tested other choices of factorization/renormalization scale μ in the calculations of $R_{p\mathrm{Pb}}(X_B)$, and found that at NLO their variations with $p_{T,\mathrm{avg}}$ are rather insensitive to the choice of μ. This is expected, since in finite-order approximation the μ-dependence of the factorized cross section is on the magnitude of the (uncalculated) higher-order contributions. For the $R_{p\mathrm{Pb}}$ defined as a ratio, the μ-dependence is further suppressed. In addition, when comparing $R_{p\mathrm{Pb}}$ to $r_i^{\mathrm{Pb}}(x_{\mathrm{Pb}}, Q^2)$ in this and previous subsections, we have approximated the values of Q^2 in r_i^{Pb} on the order of the kinematic energy scales of the hard process for a reasonable comparison. In calculations for cross sections, μ is taken on the same order of energy scale to ensure the efficacy of the perturbation theory.

All in all, the results in this subsection demonstrate the advantage of the triple-differential measurement binned with $\{X_B, E_T^{JJ}, p_{T,\mathrm{avg}}\}$ for a detailed kinematic scan of the underlying nuclear modification $r_i^{\mathrm{Pb}}(x_{\mathrm{Pb}}, Q^2)$, including both the x_{Pb} and Q^2 dependence.

IV. SUMMARY AND DISCUSSION

The deviations of the nuclear parton distributions from those of a free nucleon, arising from the additional nonperturbative dynamics that bind the nucleons together, can be generally quantified as the correction factors $r_i^A(x, Q^2) = f_i^{A,p}(x, Q^2)/f_i^p(x, Q^2)$ as functions of the nuclear mass number A, parton flavor i, momentum fraction x and resolution scale Q^2. An irreplaceable approach to accessing the corrections is to extract $r_i^A(x, Q^2)$ from the experimental measurements, relying on the factorization in perturbative QCD. In a realistic observable (e.g., a differential cross section), nuclear effects from different x regions, at different probing scales, and for various parton

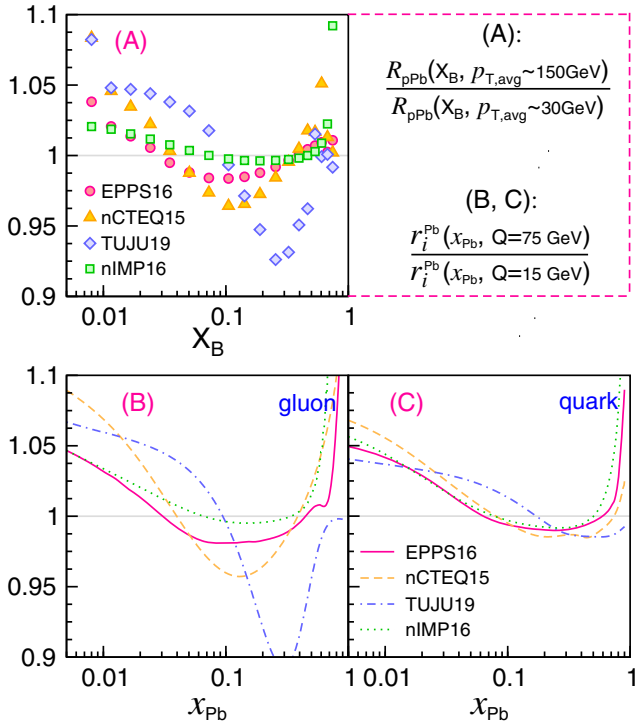

FIG. 14. Panel (A): ratio of $R_{p\mathrm{Pb}}(X_B)$ in two regions of $p_{T,\mathrm{avg}}$, i.e., $p_{T,\mathrm{avg}} \in [150, 200]$ GeV and [30, 40] GeV, corresponding to panels (B0) and (C0) in Fig. 13. Panels (B) and (C): ratios of nPDFs factors $r_i^{\mathrm{Pb}}(x_{\mathrm{Pb}}, Q^2)$ at two values of Q (75 and 15 GeV, taken as $Q \sim p_{T,\mathrm{avg}}/2$), for gluon (B) and total quark (C) distributions, respectively.

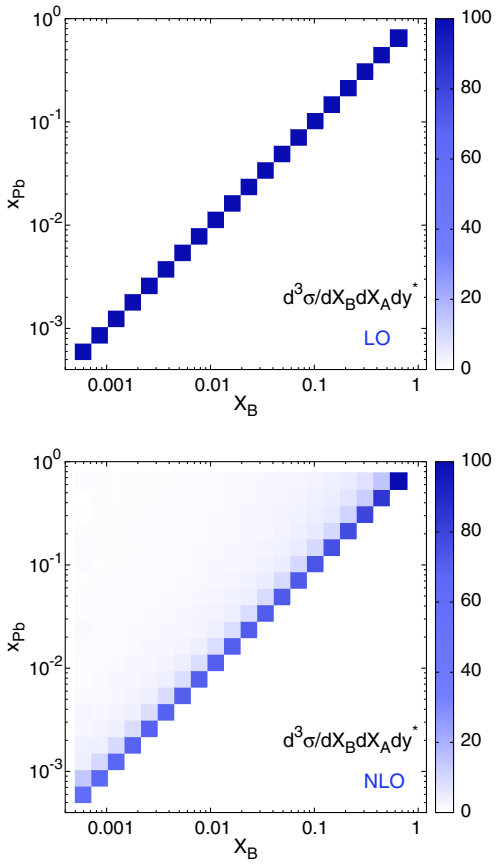

FIG. 15. Kinematic coverages of sampled dijet events in LO (top panel) and NLO (bottom panel) calculations, binned with X_B and x_{Pb}, corresponding to results in Fig. 9. For each X_B bin, total amount of dijet events with various values of x_{Pb} in the considered region $x_{\mathrm{Pb}} \in [5 \times 10^{-4}, 0.78]$ is normalized to be unity (100%).

flavors usually mix together. However, a properly defined observable that can faithfully resolve both x and Q^2 at LO level, may provide a more effective and detailed kinematic scan of the x and Q^2 dependence of $r_i^A(x, Q^2)$.

In this work, we focus on the dijet production in pPb collisions at the LHC as a probe of the nuclear quark and gluon distributions. In order to well resolve the momentum fractions of initial-state partons as well as the probing scale, we study several types of triple-differential cross sections in pp and pPb collisions, including those binned with dijet variables $V^{(3)} = \{p_{T,\mathrm{avg}}, y_b, y^*\}$, $\{X_B, X_A, y^*\}$, and $\{X_B, E_T^{JJ}, p_{T,\mathrm{avg}}\}$. These cross sections are calculated to

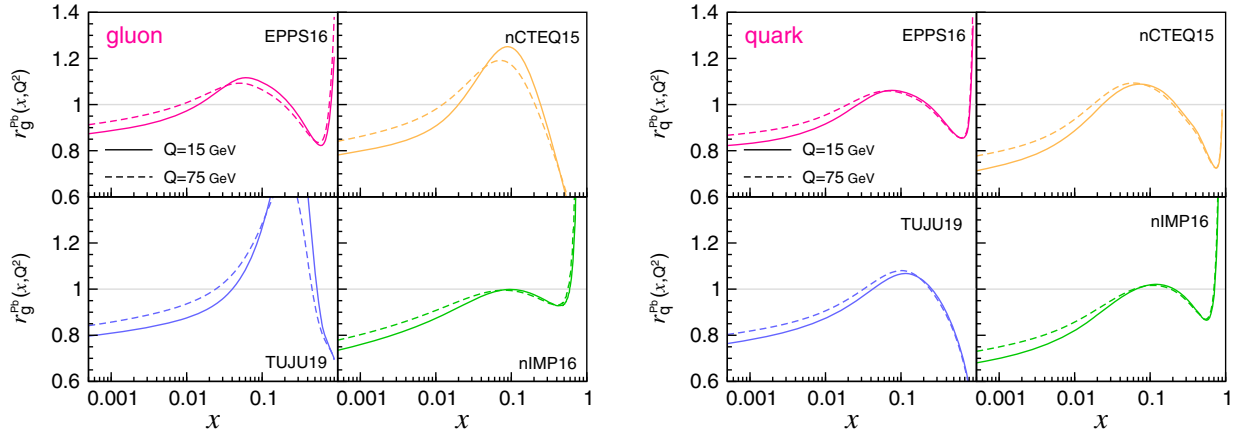

FIG. 16. Nuclear correction factors $r_i^{\mathrm{Pb}}(x, Q^2)$ for gluon (left half) and total-quark (right half) distributions at $Q = 15$ and 75 GeV from four nPDF sets, EPPS16, nCTEQ15, TUJU19, and nIMP16.

NLO in perturbative QCD. Four sets of nPDFs, EPPS16, nCTEQ15, TUJU19, and nIMParton16 are employed in the calculations for pPb. The observable nuclear modification factors $R_{p\mathrm{Pb}}$ of the triple-differential cross sections, especially those as functions of X_B, are found to provide a nice image of the nPDF correction factors $r_i^A(x, Q^2)$ from small to large values of x. Based on this, the differences among the $R_{p\mathrm{Pb}}$ predicted by various nPDFs can be well interpreted. In particular, with $V^{(3)} = \{X_B, E_T^{JJ}, p_{T,\mathrm{avg}}\}$, the variation of $R_{p\mathrm{Pb}}$ with $p_{T,\mathrm{avg}}$ can even reflect the subtle scale variation of $r_i^A(x, Q^2)$.

In future, the measurements of these $R_{p\mathrm{Pb}}$ of triple-differential dijet cross sections at the LHC with a high precision are expected to provide significant and multi-dimensional constraints on various parametrization sets of nPDFs. More importantly, the measurements will provide an effective way to help confirm various nuclear effects, e.g., shadowing, antishadowing, EMC, and Fermi motion in different regions of x and their variations with probing scale Q^2. It is also noteworthy that, the studied triple-differential cross sections can be straightforward generalized and applied to the study of other processes, such as vector-boson-tagged jet production [53–55] and heavy-quark dijet production [56]. We also hope the more accurate description of the initial-state cold nuclear matter effects provides a baseline to better understand the final-state jet quenching phenomena in relativistic heavy-ion collisions.

ACKNOWLEDGMENTS

The authors would like to thank E. Wang, H.-Z. Zhang, H. Xing, Y.-C. He, W. Dai, S.-Y. Chen, G.-Y. Ma, S.-L. Zhang, S. Wang, and Y. Luo for helpful discussions. This research was supported in part by Guangdong Major Project of Basic and Applied Basic Research No. 2020B0301030008, by Natural Science Foundation of China (NSFC) under Project No. 11935007, and by Science and Technology Program of Guangzhou (No. 2019050001). P. R. is supported by China Postdoctoral Science Foundation under Project No. 2019M652929, and the MOE Key Laboratory of Quark and Lepton Physics (CCNU) under Project No. QLPL201802.

APPENDIX A: CORRESPONDENCE BETWEEN X_B AND x_{Pb} AT NLO

In Fig. 9, we have shown the correlations between the dijet variable X_B and the momentum fraction x_{Pb} carried by the initial-state nuclear parton in pPb collisions calculated at LO. As has been discussed, this linear correspondence will be smeared to some extent once the higher-order contributions are considered. However, the intuitive demonstration in Fig. 9 (and similar ones in Figs. 5 and 11) can not be straightforward extended beyond LO within the fixed-order calculations, since the restriction imposed on the value of x_{Pb} can result in the uncanceled singularities in the calculation of dijet cross section in a certain two-dimensional bin defined with X_B and x_{Pb}. The high-order smearing may be effectively shown with an event generator including the parton showers, which we may leave to a future work.

As an alternative, the kinematic correspondence between X_B and x_{Pb} at NLO can be reflected by counting the occurrence frequency of the dijet events sampled in the calculation within the current framework. In Fig. 15, we illustrate the kinematic coverages of the sampled dijet events in both LO and NLO calculations for the cross section $d^3\sigma/dX_B dX_A dy^*$, binned with X_B and x_{Pb}. Due to the simple linear correspondence, the kinematic coverage at LO is consistent with the form in Fig. 9. At NLO, the coverage along the diagonal $X_B = x_{\mathrm{Pb}}$ is still pronounced, while the dijet events can spread into the region $X_B \leq x_{\mathrm{Pb}}$ as is expected.

It should be mentioned that, although the kinematic correspondence shown in Fig. 15 does not fully reflect the NLO contributions, the NLO results shown in Figs. 10 and 13 demonstrate to some extent that the LO relation $X_B = x_{\mathrm{Pb}}$ is a good approximation when one is comparing the $R_{p\mathrm{Pb}}(X_B)$ to the nPDF factors $r_i^{\mathrm{Pb}}(x_{\mathrm{Pb}})$.

APPENDIX B: VARIATION OF $r_i^{Pb}(x,Q^2)$ WITH Q^2

Since both the free-nucleon and nuclear PDFs evolve with the resolution scale Q^2, the nuclear correction factor $r_i^A(x, Q^2)$, i.e., the ratio of them, generally depends on Q^2. To visualize the variations of $r_i^A(x, Q^2)$ with Q^2, we supplement in Fig. 16 the $r_i^{\mathrm{Pb}}(x, Q^2)$ for gluon and quark distributions at $Q = 15$ GeV and 75 GeV, from four nPDF sets used in this work.

[1] H. Paukkunen, Proc. Sci., HardProbes2018 (**2018**) 014 [arXiv:1811.01976].
[2] K. Kovařík, P. M. Nadolsky, and D. E. Soper, Rev. Mod. Phys. **92**, 045003 (2020).
[3] M. Arneodo, Phys. Rep. **240**, 301 (1994).
[4] S. A. Kulagin and R. Petti, Nucl. Phys. **A765**, 126 (2006).
[5] N. Armesto, J. Phys. G **32**, R367 (2006).
[6] I. C. Cloet, W. Bentz, and A. W. Thomas, Phys. Rev. Lett. **109**, 182301 (2012).

[7] P. Ru, S. A. Kulagin, R. Petti, and B. W. Zhang, Phys. Rev. D **94**, 113013 (2016).
[8] B. Schmookler *et al.* (CLAS Collaboration), Nature (London) **566**, 354 (2019).
[9] X. G. Wang, A. W. Thomas, and W. Melnitchouk, Phys. Rev. Lett. **125**, 262002 (2020).
[10] M. Gyulassy, I. Vitev, X. N. Wang, and B. W. Zhang, *Jet Quenching and Radiative Energy Loss in Dense Nuclear Matter* (World Scientific, Singapore, 2004).
[11] S. Cao and X. N. Wang, Rep. Prog. Phys. **84**, 024301 (2021).
[12] M. Hirai, S. Kumano, and T. H. Nagai, Phys. Rev. C **76**, 065207 (2007).
[13] K. J. Eskola, H. Paukkunen, and C. A. Salgado, J. High Energy Phys. 04 (2009) 065.
[14] D. de Florian, R. Sassot, P. Zurita, and M. Stratmann, Phys. Rev. D **85**, 074028 (2012).
[15] K. Kovarik, A. Kusina, T. Jezo, D. B. Clark, C. Keppel, F. Lyonnet, J. G. Morfin, F. I. Olness, J. F. Owens, I. Schienbein *et al.*, Phys. Rev. D **93**, 085037 (2016).
[16] R. Wang, X. Chen, and Q. Fu, Nucl. Phys. **B920**, 1 (2017).
[17] K. J. Eskola, P. Paakkinen, H. Paukkunen, and C. A. Salgado, Eur. Phys. J. C **77**, 163 (2017).
[18] M. Walt, I. Helenius, and W. Vogelsang, Phys. Rev. D **100**, 096015 (2019).
[19] R. Abdul Khalek, J. J. Ethier, J. Rojo, and G. van Weelden, J. High Energy Phys. 09 (2020) 183.
[20] H. Khanpour, M. Soleymaninia, S. Atashbar Tehrani, H. Spiesberger, and V. Guzey, Phys. Rev. D **104**, 034010 (2021).
[21] A. Kusina, J. P. Lansberg, I. Schienbein, and H. S. Shao, Phys. Rev. D **104**, 014010 (2021).
[22] E. P. Segarra, T. Ježo, A. Accardi, P. Duwentäster, O. Hen, T. J. Hobbs, C. Keppel, M. Klasen, K. Kovařík, A. Kusina *et al.*, Phys. Rev. D **103**, 114015 (2021).
[23] K. J. Eskola, P. Paakkinen, H. Paukkunen, and C. A. Salgado, arXiv:2106.13661.
[24] R. K. Ellis, W. J. Stirling, and B. R. Webber, *QCD and Collider Physics* (Cambridge University Press, Cambridge, England, 2003).
[25] A. M. Sirunyan *et al.* (CMS Collaboration), Phys. Rev. Lett. **121**, 062002 (2018).
[26] H. Paukkunen and C. A. Salgado, J. High Energy Phys. 03 (2011) 071.
[27] P. Ru, B. W. Zhang, L. Cheng, E. Wang, and W. N. Zhang, J. Phys. G **42**, 085104 (2015).
[28] P. Ru, B. W. Zhang, E. Wang, and W. N. Zhang, Eur. Phys. J. C **75**, 426 (2015).
[29] J. L. Albacete, N. Armesto, R. Baier, G. G. Barnafoldi, J. Barrette, S. De, W. T. Deng, A. Dumitru, K. Dusling, K. J. Eskola *et al.*, Int. J. Mod. Phys. E **22**, 1330007 (2013).
[30] K. J. Eskola, P. Paakkinen, and H. Paukkunen, Eur. Phys. J. C **79**, 511 (2019).
[31] A. Kusina, J. P. Lansberg, I. Schienbein, and H. S. Shao, Phys. Rev. Lett. **121**, 052004 (2018).
[32] K. J. Eskola, I. Helenius, P. Paakkinen, and H. Paukkunen, J. High Energy Phys. 05 (2020) 037.
[33] S. D. Ellis, Z. Kunszt, and D. E. Soper, Phys. Rev. Lett. **69**, 1496 (1992).
[34] Z. Kunszt and D. E. Soper, Phys. Rev. D **46**, 192 (1992).
[35] S. D. Ellis and D. E. Soper, Phys. Rev. Lett. **74**, 5182 (1995).
[36] Z. Nagy, Phys. Rev. Lett. **88**, 122003 (2002).
[37] Z. Nagy, Phys. Rev. D **68**, 094002 (2003).
[38] J. Gao, Z. Liang, D. E. Soper, H. L. Lai, P. M. Nadolsky, and C. P. Yuan, Comput. Phys. Commun. **184**, 1626 (2013).
[39] A. Gehrmann-De Ridder, T. Gehrmann, E. W. N. Glover, A. Huss, and J. Pires, Phys. Rev. Lett. **123**, 102001 (2019).
[40] Y. He, B. W. Zhang, and E. Wang, Eur. Phys. J. C **72**, 1904 (2012).
[41] K. J. Eskola, H. Paukkunen, and C. A. Salgado, J. High Energy Phys. 10 (2013) 213.
[42] A. M. Sirunyan *et al.* (CMS Collaboration), Eur. Phys. J. C **77**, 746 (2017).
[43] S. Dulat, T. J. Hou, J. Gao, M. Guzzi, J. Huston, P. Nadolsky, J. Pumplin, C. Schmidt, D. Stump, and C. P. Yuan, Phys. Rev. D **93**, 033006 (2016).
[44] J. L. Albacete, F. Arleo, G. G. Barnaföldi, G. Bíró, D. d'Enterria, B. Ducloué, K. J. Eskola, E. G. Ferreiro, M. Gyulassy, S. M. Harangozó *et al.*, Nucl. Phys. **A972**, 18 (2018).
[45] Z. B. Kang, E. Wang, X. N. Wang, and H. Xing, Phys. Rev. Lett. **112**, 102001 (2014).
[46] P. Ru, Z. B. Kang, E. Wang, H. Xing, and B. W. Zhang, Phys. Rev. D **103**, L031901 (2021).
[47] M. Xie, X. N. Wang, and H. Z. Zhang, Phys. Rev. C **103**, 034911 (2021).
[48] A. Huss, A. Kurkela, A. Mazeliauskas, R. Paatelainen, W. van der Schee, and U. A. Wiedemann, Phys. Rev. C **103**, 054903 (2021).
[49] R. Aaij *et al.* (LHCb Collaboration), Phys. Lett. B **774**, 159 (2017).
[50] J. Arrington, J. Bane, A. Daniel, N. Fomin, D. Gaskell, J. Seely, R. Asaturyan, F. Benmokhtar, W. Boeglin, P. Bosted *et al.*, Phys. Rev. C **104**, 065203 (2021).
[51] M. S. Athar, S. K. Singh, and F. Zaidi, Phys. Rev. D **105**, 093002 (2022).
[52] J. C. Collins, D. E. Soper, and G. F. Sterman, Adv. Ser. Dir. High Energy Phys. **5**, 1 (1989).
[53] S. L. Zhang, T. Luo, X. N. Wang, and B. W. Zhang, Phys. Rev. C **98**, 021901 (2018).
[54] G. Y. Ma, W. Dai, and B. W. Zhang, Chin. Phys. C **43**, 044104 (2019).
[55] S. L. Zhang, X. N. Wang, and B. W. Zhang, Phys. Rev. C **105**, 054902 (2022).
[56] W. Dai, S. Wang, S. L. Zhang, B. W. Zhang, and E. Wang, Chin. Phys. C **44**, 104105 (2020).